


Type-II corner modes in topoelectrical circuitsS. M. Rafi-Ul-Islam ^{1,*}, Zhuo Bin Siu,^{1,†} Haydar Sahin ^{1,2,‡} and Mansoor B. A. Jalil ^{1,§}¹*Department of Electrical and Computer Engineering, National University of Singapore, Singapore 117583*²*Institute of High Performance Computing, A*STAR, Singapore 138632*

(Received 3 September 2021; accepted 1 December 2022; published 16 December 2022)

We study the rich properties of a topoelectrical (TE) circuit array consisting of lossless basic electrical components, such as capacitors and inductors, which can be designed to exhibit higher-order topological phases (HOTP). The HOTP of the circuit exhibits the characteristics of higher-order topology, i.e., unconventional bulk-boundary correspondence with strongly localized corner modes, and higher winding numbers. More interestingly, a type-II corner mode emerges in the presence of long-range interaction, which is realized in the TE circuit by the introduction of next-nearest neighbor (NNN) coupling capacitances. Unlike the usual (i.e., “type-I”) corner modes that are localized at a particular sublattice node due to the chiral symmetry, the type-II corner modes possess a spatial extent with an exponential decay length. We analytically derive this decay length as a function of the circuit parameters. The NNN coupling is also associated with the tilt parameter in the admittance spectrum of the circuit. The admittance spectrum is reminiscent of that of Dirac fermions. Changing the tilt parameter can lead to a transition from the type-I to the overtilted type-II Dirac dispersion. This overtilting results in a hybridization of the bulk and corner modes in which the distinct corner modes disappear. Furthermore, the type-I and type-II corner modes can be distinguished by their impedance readout. By virtue of their flexibility, the TE circuits provide an ideal platform to demonstrate unusual features of HOTPs arising from long-range interactions, and to engineer different types of robust topological corner modes.

DOI: [10.1103/PhysRevB.106.245128](https://doi.org/10.1103/PhysRevB.106.245128)**I. INTRODUCTION**

Topological phases in condensed matter constitute a fast emerging topic in contemporary physics [1–4] on account of their exotic characteristics such as unidirectional transport [5], spin and valley Hall effects [6–10], quantized conductances [11–13], and boundary states [14], which exhibit robustness owing to topological protection [15]. The underlying physics of the topological structure of matter is general and transcends quantum theory, being ultimately based on the properties of the parameter space [16,17]. Hence, topological phases and band structures are not just confined to condensed matter systems. Starting from the pioneering work of Haldane [18], such topological phenomena have been observed in a multitude of seemingly unrelated settings, e.g., photonic systems [19,20], ultracold atomic gases in optical lattices [21], mechanical systems [22], acoustic systems [23], plasmonic systems [24], microcavities [25], and optical waveguides [26]. Conventionally, topological phases exhibit a boundary state with a dimensionality of one less than that of the system, e.g., a topological phase in a three-dimensional system would sport a two-dimensional (surface) boundary state. Recently this concept of bulk-boundary correspondence has been generalized to higher-order topological phases (HOTPs) [27–31],

where an n -order topological phase is associated with a higher topological invariant for $n > 1$, and has a boundary state of dimensionality $(d - n)$ where d is the system dimensionality. To date, HOTPs have also been demonstrated in various platforms including microwave [32], photonics [33], acoustics [31], and optical lattice [34] systems. In two- or three-dimensional systems, the boundary state may take the form of corner states.

Recently, the effects of long-range interactions on the topological characteristics of the Lieb [35] and Kagome lattices [36] have been investigated in photonic structures [36–38]. However, the effect of long-range interactions has not been fully investigated, such as the estimation of the decay rate of corner modes in the presence of NNN coupling. In addition, it is not straightforward to modulate the strength and form of the long-range interactions in the aforementioned photonic platforms. In this paper, we will analyze the role of long-range interactions on HOTPs and their corner modes based on a newly established platform known as topoelectrical (TE) circuits [39–46], which is based on electrical components. Research in TE circuits has built a bridge between the two different domains of circuit theory on one hand and quantum theory and topology on the other [40,42,43,43,47–50]. The accessibility and ubiquity of basic circuit components would presage efficient and accurate practical modeling of various topological phenomena via TE circuits [50–52]. Moreover, one can readily incorporate long-range interactions in TE circuits by means of couplings beyond the nearest neighboring nodes. In addition, the resonant electrical responses of a TE circuit can serve as signatures

*e0021595@u.nus.edu

†elesiu@nus.edu.sg

‡sahin@nus.edu.sg

§lembaj@nus.edu.sg

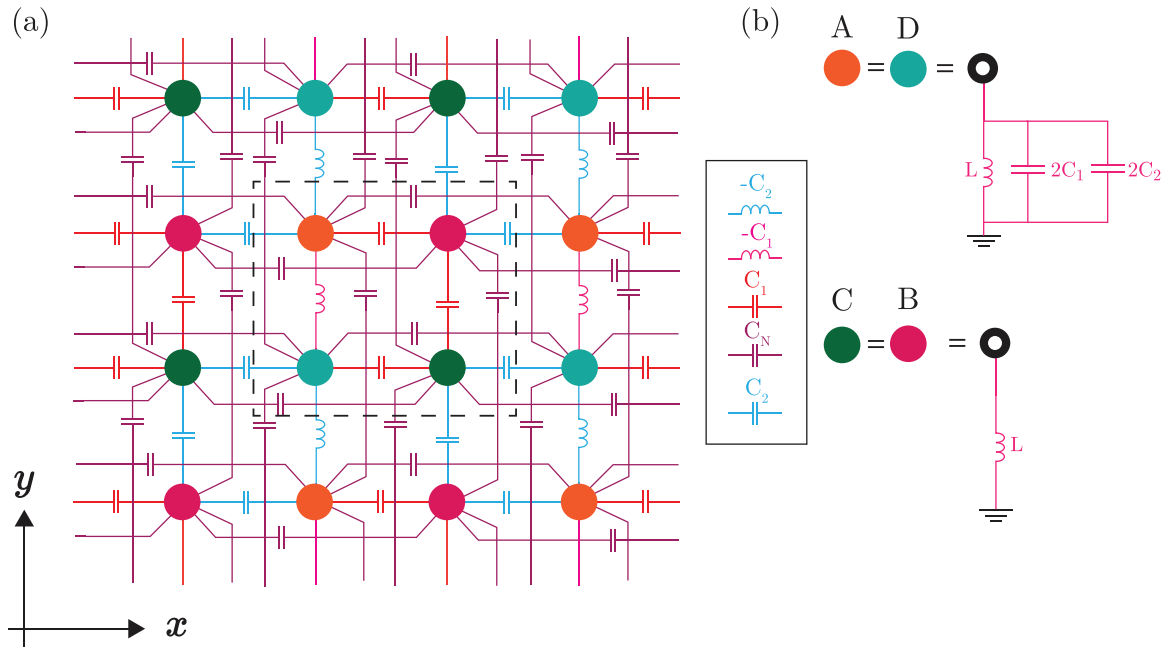


FIG. 1. Topoelectrical circuit model that hosts higher-order topological phases with type-II corner modes. Here the orange, magenta, green, and cyan circles denote the A, B, C, and D sublattice nodes, respectively. (a) Circuit array consisting of capacitors and inductors. (The unit cell is delineated by a dashed rectangle.) The capacitor C_1 denotes intracell coupling while C_2 and C_N represent the intercell and the next-nearest nodes coupling, respectively. Note that the capacitive couplings can take negative values, in which case they correspond to frequency-dependent inductances in the physical circuit [i.e., $-C_i = -(\omega^2 L_i)^{-1}$]. (b) Grounding mechanism of our TE circuit. All nodes are connected to the ground by a common capacitor inductor (L). Furthermore, two parallel capacitors of $2C_1$ and $2C_2$ connect the A and B nodes to the ground to ensure uniform diagonal terms in the Laplacian matrix throughout the whole circuit.

of the boundary modes of the resulting topological systems [40]. In view of these advantages, the TE circuit framework is employed in our study on the effect of long-range interactions on HOTPs and their corner modes. Recently, long-range coupling has been investigated in a quadrupolar system [53] implemented on an electrical platform where the chiral symmetry breaking induces an indirect gap phase, which makes it difficult to distinguish the corner modes from the bulk bands, hence destroying the topological quadrupole phase.

In this work, we theoretically propose a TE circuit based on a modified two-dimensional SSH model which hosts higher-order topological phases (HOTPs) with corner modes. We demonstrate the emergence of “type-II” corner modes [20,54] due to the introduction of next-nearest neighbor (NNN) coupling in the circuit lattice. The effects of long-distance couplings on corner modes have earlier been studied in a different system in Ref. [38]. The corner modes in our system have a finite spatial extent with probability density profiles that exponentially decay at much slower rates away from the corner nodes due to the broken chiral symmetry compared to the conventional “type-I” corner modes, which are localized on a particular lattice site (i.e., corner modes) with very large inverse decay lengths (of infinity in the thermodynamic limit) and protected by chiral symmetry. In contrast, the long-range NNN coupling breaks chiral symmetry and also results in the tilting of the Dirac fermionlike admittance dispersion. Beyond a critical NNN coupling strength, the admittance dispersion assumes an overtilted form, leading to the disappearance of the corner modes due to their hybridization with the bulk

modes. Our TE-based analysis of the effect of long-range coupling on the topological corner modes demonstrates the applicability of these circuits to model higher-order topological phases. The fact that these circuits are readily tunable and implemented in practice, e.g., by using established printed circuit board technology, opens a new avenue for the accessible modeling and realization of higher-order topological phases prior to their translation to other (e.g., condensed matter) platforms.

II. TOPOELECTRICAL CIRCUIT MODEL

Consider a periodic two-dimensional topoelectrical circuit lattice consisting of lossless capacitances and inductances as shown in Fig. 1. As will be shown later, the lattice can potentially host a higher-order topological phase (HOTP) and associated corner modes, which are protected by certain symmetries. The unit cell of the circuit consists of four different types of sublattice nodes labeled as A, B, C, and D, which are denoted as orange, magenta, green, and cyan circles in Fig. 1(a), respectively. The intracell and intercell hopping amplitudes are denoted by C_1 and C_2 , respectively. Note that the coupling capacitance can assume a negative value, which corresponds to a frequency-dependent inductive coupling in a physical circuit. We incorporate a long-range electrical coupling by connecting the nondiagonal next-nearest neighboring (NNN) nodes with coupling capacitors C_N . (We call the C_N coupling a NNN coupling because the nodes coupled together are separated by nearest neighbor coupling nodes. For example, the D NNN nodes are separated by a C NN node along the

x direction and a A NN node along the y direction.) Thus, in general, the amplitude and phase of the coupling between the different nodes in the TE circuit can be tuned by adjusting the capacitance/inductance coupling between the nodes. All the electrical nodes are connected to the ground via an inductor L . As we shall see later, the common inductor L sets the diagonal elements of the admittance matrix of the circuit and thus its resonant frequency condition. Furthermore, to ensure that all the diagonal elements in the Laplacian matrix assume the same value, additional grounding capacitances of $2C_1$ and $2C_2$ are connected in parallel to the other grounding capacitances for the type A and D nodes, as depicted in Fig. 1(b). The enforced uniformity of the diagonal elements in the Laplacian matrix is analogous to setting the on-site energies of all the lattice sites to the same value, so that there is effectively no potential energy difference between one site relative to another.

A. Circuit Laplacian

The Laplacian of the higher order TE circuit model shown in Fig. 1 (divided by $i\omega$, where ω is the angular frequency of the driving current), which is analogous to the tight-binding Hamiltonian model, can be expressed as

$$\begin{aligned}
 -J_{\text{TE}}(k_x, k_y) = & 2C_N[\cos(k_x) + \cos(k_y)]\sigma_0 \otimes \sigma_0 + [C_1 \\
 & + C_2 \cos(k_x)]\sigma_0 \otimes \sigma_x + C_2 \sin(k_x)\sigma_z \otimes \sigma_y \\
 & + [C_1 + C_2 \cos(k_y)]\sigma_y \otimes \sigma_y + C_2 \sin(k_y)\sigma_x \\
 & \otimes \sigma_y - \left(2(C_1 + C_2 + 2C_N) - \frac{1}{\omega^2 L}\right)\sigma_0 \otimes \sigma_0
 \end{aligned} \quad (1)$$

in the (A,B,C,D) node basis where $\sigma = (\sigma_x, \sigma_y, \sigma_z)$ are the Pauli matrices, C_i and $-C_i$ denote the capacitive and inductive coupling strengths between different sublattice sites, respectively, and the resonant frequency is given by $\omega_r = 1/\sqrt{2(C_1 + C_2 + 2C_N)L}$. C_N represents the long-range NNN hopping amplitude along both the x and y directions. The eigenvalues of the Laplacian can be expressed as

$$\begin{aligned}
 E_{\text{TE}} = & 2C_N[\cos(k_x) + \cos(k_y)] \\
 & \pm \sqrt{2\{C_1^2 + C_2^2 + C_1 C_2[\cos(k_x) + \cos(k_y)]\}}.
 \end{aligned} \quad (2)$$

Note that the Laplacian in Eq. (1) is a four-by-four matrix but there are only two distinct values of the eigenvalues in Eq. (2), which implies a twofold degeneracy in the admittance values. In the absence of NNN coupling, i.e., when $C_N = 0$, the admittance equation resembles that of the Benalcazar-Bernevig-Hughes (BBH) model [55–58] and hence shows two distinguishable topological phases, i.e., the trivial and nontrivial phases for $|C_1/C_2| > 1$ and $|C_1/C_2| < 1$, respectively. Interestingly, at the phase transition point ($C_1 = \pm C_2$), the bulk admittance gap closes at either $(k_x, k_y) = (\pi, \pi)$ or $(0,0)$ depending on the sign of C_1/C_2 . In the presence of only NN hopping, the Laplacian in Eq. (1) satisfies chiral symmetry, i.e., $\Theta J_{\text{TE}}(k_x, k_y)\Theta^{-1} = -J_{\text{TE}}(k_x, k_y)$ with $\Theta = \sigma_0 \otimes \sigma_z$. This chiral symmetry is broken with the incorporation of NNN coupling. However, the Laplacian with C_N still

obeys the reflection symmetries along x and y direction with $M_x J_{\text{TE}}(k_x, k_y) M_x^{-1} = J_{\text{TE}}(-k_x, k_y)$ and $M_y J_{\text{TE}}(k_x, k_y) M_y^{-1} = J_{\text{TE}}(k_x, -k_y)$, where $M_x = \sigma_z \otimes \sigma_x$ and $M_y = \sigma_x \otimes \sigma_x$ are the reflection operators along the x and y directions, respectively. Interestingly, M_x and M_y do not commute with each other, i.e., $M_x \cdot M_y \neq M_y \cdot M_x$.

B. Admittance dispersion

To illustrate the behavior of the system, we study the evolution of the admittance dispersion of the TE system and the spatial distribution of its eigenmodes when the width of the system is made finite (20 unit cell width) first in the y direction and then in both the x and y directions (see Fig. 2). Figure 2(a) shows the dispersion relation for a TE circuit with periodic boundary conditions along both the x and y directions and $C_1 = 0.5$ mF, $C_2 = 1$ mF, and $C_N = 0.3(C_2/\sqrt{2})$. For this set of parameters, there are well-separated upper and lower bands corresponding to the \pm branches of Eq. (2). The bands exhibit the aforementioned x and y reflection symmetries. The presence of the long-range coupling C_N breaks the chiral symmetry between the upper and lower bands. Figure 2(b) shows the admittance dispersion of the TE circuit in a nanoribbon geometry, i.e., infinite along the x direction with periodic boundary conditions (PBC), and with a finite width of 20 unit cells and open boundary conditions along the y direction. The finite width along the y direction leads to the emergence of discrete subbands in the dispersion relation. The fact that these are bulk bands can be ascertained from the voltage amplitude profile of the eigenmodes in the band (note that the voltage amplitude profile is the TE analog of the quantum mechanical particle density). Consider, for example, the $k_x = 0$ mode corresponding to the lowest eigenmode in the top bulk band and labeled as P in Fig. 2(b). As shown in the upper inset of Fig. 2(b), this eigenmode has a voltage amplitude with a significant distribution within the interior of the nanoribbon. In addition to the quantized bulk modes, topological edge modes, denoted by the thicker line in the dispersion relation, emerge inside the bulk band gap between the quantized upper and lower bulk bands. These edge modes are localized near the edges of the nanoribbon, as exemplified by the $k_x = 0$ mode corresponding to the edge band and labeled as Q. As plotted in the lower inset of Fig. 2(b), the voltage profile for this mode shows significant localization at both edges. Finally, Fig. 2(c) shows the admittance eigenvalues of the TE circuit in a nanoplate geometry, i.e., with finite widths of 20 unit cells along both the x and y directions, and open boundary conditions in both. The confinement along both in-plane directions leads to discrete eigenvalues, which are plotted besides part of the dispersion of Fig. 2(b) corresponding to the nanoribbon geometry. Some of these eigenvalues fall within the admittance ranges of the nanoribbon bulk and edge modes. These are exemplified by the modes labeled as R and T, respectively. Mode R is “bulklike” with a voltage profile distribution that is mostly confined in the interior of the nanoplate, while mode T has “edgelike” characteristics with its voltage distribution being confined along the edges of the nanoplate. In addition to these bulk and edgelike modes, additional topological modes emerge in the nanoplate geometry that have no counterparts in the nanoribbon geometry, and thus fall within the gaps

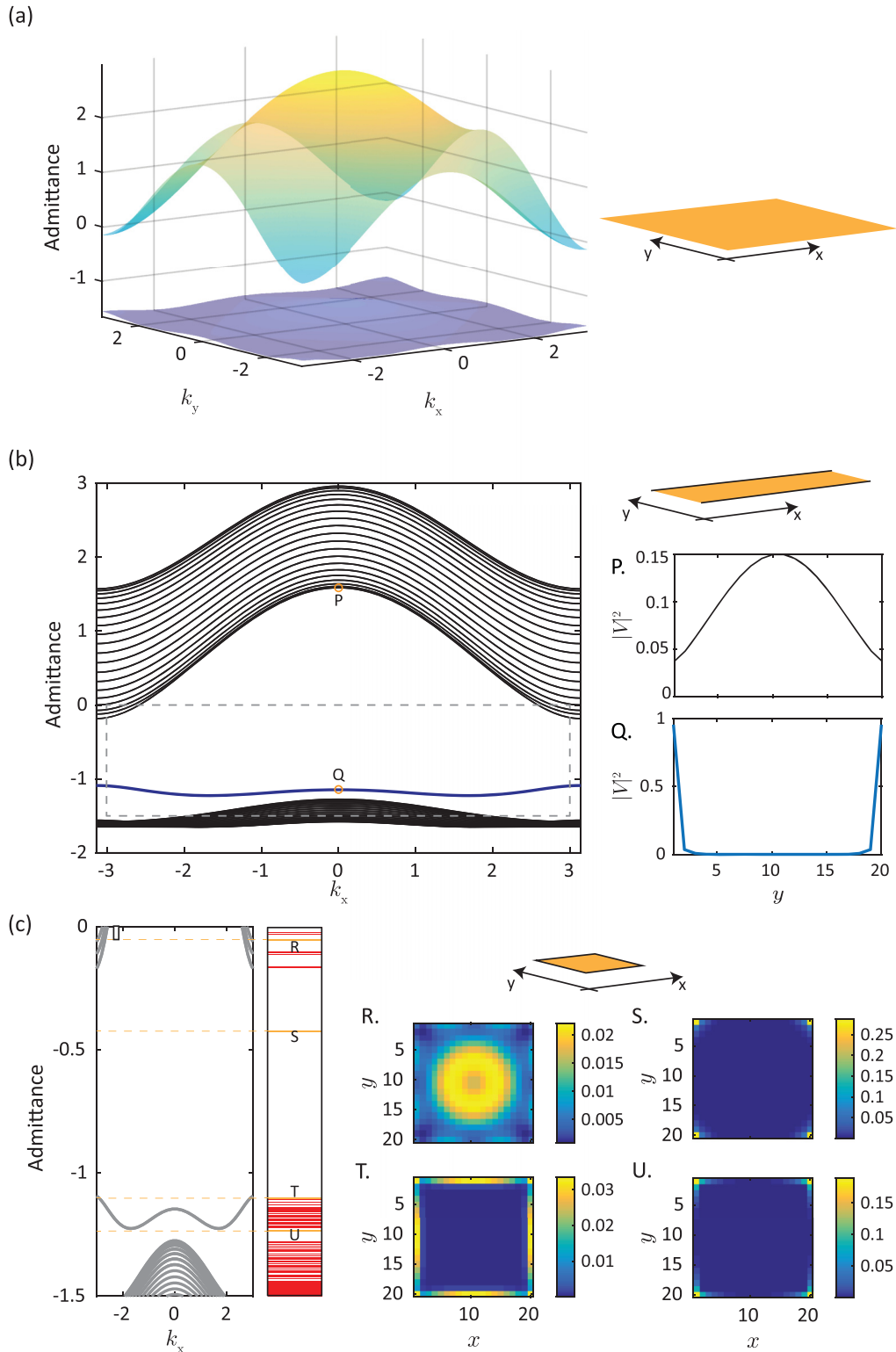


FIG. 2. (a) Dispersion relation of a TE circuit with periodic boundary conditions along both the x and y directions, and $C_1 = 0.5$ mF, $C_2 = 1$ mF, and $C_N = 0.3(C_2/\sqrt{2})$. (b) Dispersion relation of the same TE circuit in a nanoribbon geometry with a finite width of 20 unit cells along the y direction and infinite width with periodic boundary conditions along the x direction. The dark blue line denotes the edge modes. The $k_x = 0$ modes labeled as P and Q in (b) are bulk and edge modes, respectively, as shown in the plots of the square of the voltage amplitude on the right. The gray box denotes the area of the dispersion plot shown in the zoomed-in view on the left of (c). (c) The red horizontal lines on the left show the discrete admittance eigenvalues of the circuit with a nanoplate geometry. The four plots show the spatial distribution of the square of the voltage amplitude over the finite (20×20) unit cell TE circuit with the nanoplate geometry. It can be clearly seen that modes R and T correspond to a bulk mode and an edge mode, respectively, while modes S and U correspond to type-II corner modes, which are localized in the vicinity of the corner nodes but exponentially decay away from them.

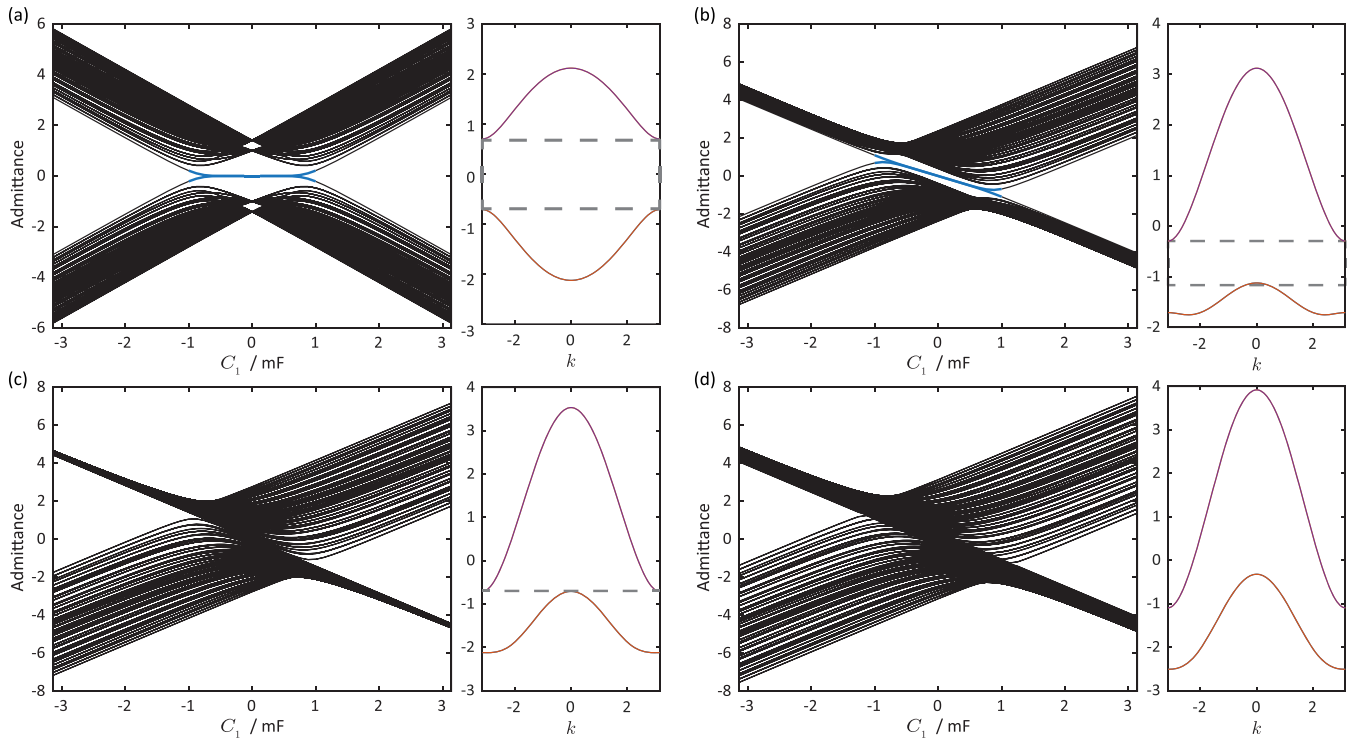


FIG. 3. The admittance spectra of a finite TE circuit array with nanoplate geometry of size 20×20 unit cells along both the x and y directions which are plotted as a function of C_1 with $C_2 = 1$ mF at four different values of NNN coupling strengths: (a) $C_N = 0$ mF, (b) $C_N = 0.25$ mF, (c) $C_N = \frac{C_2}{2\sqrt{2}} = 0.35355$ mF, and (d) $C_N = 0.45$ mF. In the secondary plot on the right of each main plot with $C_1 = 0.5$ mF and $C_2 = 1.0$ mF, the admittance spectrum is plotted along the direction $k_x = k_y = k$ for an infinite TE circuit with periodic boundary conditions along the x and y directions and the same corresponding values of C_N , C_1 and C_2 . The thick blue lines in the main plots in (a) and (b) denote the corner modes. The dotted lines on the right mark the maxima of the upper bands and the minima of the lower bands.

between the bulk and edge modes of the nanoribbon. These additional modes are the corner modes, as exemplified by the modes labeled as S and U. Unlike the more familiar edge modes which have an approximately constant amplitude along the length of each edge on the nanoplate, the voltage amplitude of the corner modes decays exponentially away from each of the four corners of the nanoplate. In this case, we obtain a new type of corner mode, which we term as type-II corner modes, where along with the typical localization at the corners, we have an exponentially decaying spatial distribution away from the corners. This higher-order topological phase is the direct result of the long-range interactions in the TE circuit which are represented by the NNN coupling. Next, we investigate the effects of C_N and the NN coupling capacitances C_1 and C_2 , as well as the long-range NNN coupling C_N on the topological edge modes in the TE circuit. In Fig. 3, we plot the admittance spectra as a function of the intracell coupling C_1 for a TE circuit with a nanoplate geometry, i.e., with a finite width of 20 unit cells along both the x and y directions for four representative values of C_N . In Fig. 3(a), we find that in the absence of C_N , there exist well-defined higher-order corner modes as depicted by the thick blue line. The circuit array hosts these topological phases for NN coupling values such that $|C_1/C_2| < 1$, while for $|C_1/C_2| > 1$, the topological modes are absent because the system is in the trivial phase. Therefore, the topological phase transition between the second-order topological and trivial phases occurs at $C_1 = C_2$. This is reminiscent of the transition between the first-order

topological and trivial phases of the SSH model. Moreover, the admittance dispersion is symmetric about zero admittance.

However, a different evolution of the boundary modes is observed with the introduction of a nonzero NNN coupling C_N in the TE circuit. Introducing a finite C_N leads to the tilting of the boundary modes as C_1 is varied [see Figs. 3(b) and 3(c)]. The admittance dispersion also becomes asymmetric with respect to the zero-admittance axis. Consider the dispersion for the same system but with periodic boundary conditions along both the x and y directions and for $C_1 = 0.5$ mF and $C_2 = 1.0$ mF, plotted along the wave-vector direction of $k_x = k_y \equiv k$ (see plot on the right of each panel). We find that at small values of C_N , an energy gap exists between the top of the upper band and the bottom of the lower band. However, at a critical value of $C_N = C_N^{\text{critical}} = C_2/(2\sqrt{2})$, the energy gap closes.

We will now discuss the gap closure and its effect on the topological corner modes. The critical NNN coupling value of $C_N = \frac{C_2}{2\sqrt{2}}$ where the corner modes touch the bulk bands [see Fig. 3(c)] can be derived as follows. At this critical value of C_N , the bottom of the upper band at $k_x = k_y = 0$ falls below the top of the lower band at $k_x = k_y = \pm\pi$, and the energy gap between the upper and lower bands vanishes. The minimum of the upper band at $k_x = k_y = \pm\pi$ is $E_+ = -4C_N + \sqrt{2}|C_1 - C_2|$, while the maximum of the lower band at $k_x = k_y = 0$ is $E_- = 4C_N - \sqrt{2}(C_1 + C_2)$ [see right panel of Fig. 3(c)]. The minimum of the upper band occurs when $C_1 = C_2$, and the lower and upper bands overlap when $E_- > E_+ \Rightarrow C_N > \frac{C_2}{2\sqrt{2}}$.

Above this critical value of C_N , the bulk and corner modes mix [see Fig. 3(d)]. At this point, the corner modes are no longer evident in the admittance spectra. The critical value of $C_N = C_N^{\text{critical}} = \frac{C_2}{2\sqrt{2}}$ can also be related to the overtilting of the admittance dispersion. The Laplacian in Eq. (1) can be block diagonalized about the high symmetry line $k_x = k_y = k$ to give

$$U^{-1}J_{2D}(k)U = \begin{pmatrix} J_+(k) & 0 \\ 0 & J_-(k) \end{pmatrix}, \quad (3)$$

where U is a unitary transformation. Such a unitary transformation can be accomplished by, for example

$$U = \begin{pmatrix} \frac{1}{\sqrt{2}} & 0 & -\frac{1}{\sqrt{2}} & 0 \\ \frac{1}{\sqrt{2}} & 0 & \frac{1}{\sqrt{2}} & 0 \\ 0 & 1 & 0 & 0 \\ 0 & 0 & 0 & 1 \end{pmatrix}. \quad (4)$$

The $J_{\pm}(k)$ matrix can be expressed as $J_{\pm}(k) = 4C_N \cos(k)\sigma_0 + \sqrt{2}[C_1 + C_2 \cos(k)]\sigma_x \pm \sqrt{2}C_2 \sin(k)\sigma_y$.

Expanding $J_{\pm}(k)$ around $k = \pi/2$,

$$J_{\pm}(q) = -4C_N q\sigma_0 + \sqrt{2}(C_1 - C_2 q)\sigma_x \pm \sqrt{2}C_2 \sigma_y, \quad (5)$$

where q is a small perturbation to $k = \pi/2$, i.e., $k = \pi/2 + q$. From Eq. (5), it is clear that the NNN capacitor gives rise to a tilt term $-4C_N q\sigma_0$ in the low-admittance Laplacian in addition to a term analogous to a one-dimensional Dirac fermion Hamiltonian $-\sqrt{2}C_2 q\sigma_x$, and q -independent terms $\sqrt{2}C_1\sigma_x \pm \sqrt{2}C_2\sigma_y$ which correspond to effective exchange couplings. With the increase of the C_N , the tilting of the ad-

mittance dispersion in \vec{k} space increases. At the critical value of $C_N = C_N^{\text{critical}} = \frac{C_2}{2\sqrt{2}}$, the tilting term $-4C_N q\sigma_0$ becomes equal in magnitude to the coefficient of $-\sqrt{2}C_2$ in the $q\sigma_x$ term corresponding to the Dirac fermion Hamiltonian, and the resulting dispersion relation becomes overtilted [59–61]. This is reminiscent of the transition from a type-I to a type-II Dirac fermion Hamiltonian [62–64]. Note that the tilt direction of the boundary modes can be switched by switching the sign of C_N through the replacement of the capacitive NNN hopping with an inductive NNN coupling.

C. Inverse localization length of type-II corner modes

We will now analyze one of the hallmark effects of the long-range coupling, i.e., the exponential decay of the corner modes and the tilt induced in the admittance dispersion by the next-nearest neighbor (NNN) coupling. Figure 4(a) shows the admittance spectrum of a TE circuit described by $J_{\text{TE}}(k_x, k_y)$ in Eq. (1) with a nanoplate geometry at different values of the NNN coupling C_N . The admittance spectrum shows an almost linear tilting of the midgap corner modes for comparatively small values of C_N . In contrast, a moderately large C_N (i.e., $C_N \geq C_N^{\text{critical}}$) results in the overlapping of different bands and vanishing of the admittance band gap signifying the insulating to metallic phase transition, as well as the mixing of the topological corner modes with the bulk modes. We will now derive the inverse localization length in the presence of C_N . We first consider the $C_N = 0$ limit for a semi-infinite system extending over $x \in (0, \infty)$, $y \in (0, \infty)$ and show the existence of the “true” or type-I normal modes in this system. The Laplacian in Eq. (1) at resonant frequency for this system in the basis $ACBD$ reduces to

$$J_{\text{TE}}|_{C_N=0} = - \begin{pmatrix} 0 & 0 & C_1 + C_2 \exp(-ik_x) & -C_1 - C_2 \exp(ik_y) \\ 0 & 0 & C_1 + C_2 \exp(-ik_y) & C_1 + C_2 \exp(ik_x) \\ C_1 + C_2 \exp(ik_x) & C_1 + C_2 \exp(ik_y) & 0 & 0 \\ -C_1 - C_2 \exp(-ik_y) & C_1 + C_2 \exp(-ik_x) & 0 & 0 \end{pmatrix}. \quad (6)$$

Consider $k_x = k_y = -i \ln(-C_1/C_2)$. When $|C_1| < |C_2|$, as is the case for the range of C_1 for which zero energy edge modes exists in Fig. 3(a), k_x and k_y have positive imaginary parts. This combination of k_x and k_y then corresponds to modes that are localized near the lower left corner of the system, and the Laplacian is reduced to

$$J_{\text{TE}}|_{C_N=0; k_x=k_y=-i \ln(-C_1/C_2)} = \left(C_1 - \frac{C_2^2}{C_1} \right) \begin{pmatrix} 0 & 0 & 1 & 0 \\ 0 & 0 & 1 & 0 \\ 0 & 0 & 0 & 0 \\ -1 & 1 & 0 & 0 \end{pmatrix}. \quad (7)$$

The Laplacian has the eigenvalue 0 and two nontrivial eigenmodes, which we denote as $\psi_{1,2}(\vec{r})$ and are explicitly given by $\psi_1(\vec{r}) = (-C_1/C_2)^{x+y} \frac{1}{\sqrt{2}}(1, 1, 0, 0)^T$ and $\psi_2(\vec{r}) = (C_1/C_2)^{x+y}(0, 0, 0, 1)^T$. The eigenmode of $k_x \rightarrow +i\infty$ is also an eigenmode of the system with the eigenvalue of 0 at $C_N = 0$. This eigenmode corresponds to a Kronecker delta-localized mode that has a finite value only at the leftmost edge of the

system [because $\exp(ik_x x) \rightarrow +\infty$ as $x \rightarrow -\infty$]. The Laplacian in Eq. (1) effectively becomes

$$J_{\text{TE}}|_{C_N=0} = C_2 \begin{pmatrix} 0 & 0 & 1 & 0 \\ 0 & 0 & 0 & 0 \\ 0 & 0 & 0 & 0 \\ 0 & 1 & 0 & 0 \end{pmatrix}, \quad (8)$$

which has the eigenvalue of 0 and the corresponding eigenvectors of $(1, 0, 0, 0)^T$ and $(0, 0, 0, 1)^T$. The corresponding spatial eigenmodes, which we denote as $\psi_{3,4}(\vec{r})$, can hence be written as $\psi_3(\vec{r}) = \delta_{x,0}(1, 0, 0, 0)^T$ and $\psi_4(\vec{r}) = \delta_{x,0}(0, 0, 0, 1)^T$. Similarly, the eigenmodes with $k_y = +\infty$ correspond to Kronecker delta-localized modes that are localized at the lower edge of the system. Their corresponding eigenmodes, which we denote as $\psi_{5,6}(\vec{r})$, are then given by $\psi_5(\vec{r}) = \delta_{y,0}(0, 1, 0, 0)^T$ and $\psi_6(\vec{r}) = \delta_{y,0}(0, 0, 0, 1)^T$. In addition, when both $k_x = k_y = +i\infty$, there are another two nontrivial eigenmodes with 0 eigenenergy that are given by $\psi_7(\vec{r}) = \delta_{x,0}\delta_{y,0}(1, 1, 0, 0)^T$ and $\psi_8(\vec{r}) = \delta_{x,0}\delta_{y,0}(0, 0, 0, 1)^T$.

Because $\psi_1(\vec{r})$ to $\psi_8(\vec{r})$ are all eigenmodes with the eigenvalue of 0, any linear combination of these eigenmodes is also an eigenmode with the same eigenvalue. In particular, the linear combination of $\psi_{\text{lower-left}}(\vec{r}) = \psi_2(\vec{r}) + \psi_8(\vec{r}) - (-C_1/C_2)^y \psi_4(\vec{r}) - (-C_1/C_2)^x \psi_6(\vec{r})$, i.e.,

$$\psi_{\text{lower-left}}(\vec{r}) = \left[\left(-\frac{C_1}{C_2} \right)^{x+y} + \delta_{x,0} \delta_{y,0} - \left(-\frac{C_1}{C_2} \right)^y \delta_{x,0} - \left(-\frac{C_1}{C_2} \right)^x \delta_{y,0} \right] \begin{pmatrix} 0 \\ 0 \\ 0 \\ 1 \end{pmatrix} \quad (9)$$

constitutes a corner mode localized at the lower-left corner with the eigenvalue of 0 satisfying the boundary conditions that the wave function vanishes along the boundaries parallel to the x and y axes, i.e., at $y = 0$ and $x = 0$, respectively. The fact that $\psi_{\text{lower-left}}(\vec{r})$ is constructed from the eigenvectors of rank-deficient Laplacians is a hallmark of a topologically non-trivial mode. $\psi_{\text{lower-left}}(\vec{r})$ represents the corner mode localized at the lower left corner of the system considered with a decay length of $\ln(|C_2/C_1|)$ in the limit of an infinite-sized system. Corner modes with the eigenvalue of 0 localized at the other three corners can also be constructed in a similar manner. This also ensures the existence of chiral symmetry of the system in the absence of C_N .

We will now consider the effect of NNN coupling in modifying the spatial distribution of the corner modes. The decay rate of the type-II corner modes increases significantly with the increase of C_N . In brief, a finite C_N results in the

replacement of the infinite imaginary k terms that gave rise to the Kronecker delta terms in Eq. (9) by finite values of $|k_{x,y}|$. This replacement occurs because the terms proportional to C_N in the diagonal elements of Eq. (1), and correspondingly the eigenvalues of the Laplacian, will go to infinity when k has infinite imaginary values. The corresponding eigenvector will then take on a more complicated expression containing more than a single nonzero component, unlike the eigenvector in Eq. (9) which contains only a single nonzero component. The admittance eigenvalue E_{corner} of the isolated corner modes can be estimated via perturbation theory [54] as

$$E_{\text{corner}} = [2(C_1 + C_2 + 2C_N) - (\omega^2 L)^{-1}] - 4C_N C_1 C_2^{-1}, \quad (10)$$

which has the form of a linear relation of the corner modes with the NNN hopping C_N . (Note that we have set the driving frequency to $f_r = \frac{1}{2\pi}(\sqrt{2(C_1 + C_2 + 2C_N)L})^{-1}$ so that the k -independent terms proportional to the 4×4 identity matrix in Eq. (1) cancel out to zero. One can also set another frequency (i.e., the driving frequency) at $\frac{1}{2\pi}(\sqrt{2(C_1 + C_2 + 2C_N - 4\frac{C_N C_1}{C_2})L})^{-1}$, where the corner modes will fall exactly on the zero-admittance line. To avoid confusion to the reader, we now do not refer to this driving frequency of $f_r = \frac{1}{2\pi}(\sqrt{2(C_1 + C_2 + 2C_N)L})^{-1}$ as “the resonant frequency” when C_N is finite but refer to it as simply as “the driving frequency.” Equation (2) can be expanded in the vicinity of $k \rightarrow \pi + i\lambda$ to determine the inverse localization length λ of the corner modes such that the relation $E_{2D} = E_{\text{corner}}$ is satisfied. Explicitly, for a given AC angular frequency of ω , λ is given by

$$\lambda = \cosh^{-1} \left(\frac{-C_1(C_2^2 + 4C_2C_N - 8C_N^2) + 2C_2C_N[\frac{1}{\omega^2 L} - 2(C_2 + 4C_N)] + C_2\sqrt{\Delta}}{8C_2C_N^2} \right), \quad (11)$$

where $\Delta = 8C_2^2C_N^2 + C_1^2(C_2^2 + 8C_2C_N - 8C_N^2) + 4C_1C_2C_N[2(C_2 + 4C_N) - \frac{1}{\omega^2 L}]$. We plot the logarithm of the inverse localization length of the corner modes in Fig. 4(b) at the resonant frequency (i.e., $\omega = \omega_r = 2\pi f_r$). As expected, the inverse localization length of the type-II corner modes falls to zero at $C_N = C_N^{\text{critical}}$, at which the admittance band gap vanishes and the bulk admittance modes become mixed with the corner modes [see Fig. 4(b)].

Note that, in our analytical derivations for Eqs. (5) to (10) in Sec. II C, we have adopted a boundary condition where the four nodes in the unit cell beyond the edge of the finite system are both zero in the presence of next-nearest coupling. Therefore, the corner modes can be expressed as a linear combination of four terms with different inverse localization length (ILL) if the coupling strengths in the x and y directions are different [65,66], as shown explicitly in Eq. (9) for the $C_N = 0$ and semi-infinite system case. Equation (9) also shows that all of these four terms contain either the common finite decay length of $\ln(|C_1/C_2|)$ along both the x/y directions and/or Kronecker-delta localizations at the edges. Equation (10) gives the finite corresponding decay length for finite C_N in a semi-infinite system. We have numerically

decomposed the corner states for the finite system shown in Fig. 2(c) into their component PBC eigenstates and found that these states are dominated by only a single finite value of the decay length.

D. Impedance spectra

In the previous section, we investigated how the admittance spectra vary with the change in NNN hopping. In this section, we evaluate the two-point impedance spectra of the HOTP circuit in Fig. 1 with long-range interactions and show that the spectra provide an accessible way to distinguish various corner mode configurations under different values of the NNN coupling capacitances. The two-node impedance of a finite electrical network can be evaluated using the Green's function method [39] as

$$Z_{pq} = \frac{1}{i\omega} \sum_j \frac{\psi_{j;p}^* \psi_{j;p} + \psi_{j;q}^* \psi_{j;q} - \psi_{j;p}^* \psi_{j;q} - \psi_{j;q}^* \psi_{j;p}}{E_j} \quad (12)$$

$$= (\mathbf{J}_{\text{TE}_{p,p}}^{-1} + \mathbf{J}_{\text{TE}_{q,q}}^{-1} - \mathbf{J}_{\text{TE}_{p,q}}^{-1} - \mathbf{J}_{\text{TE}_{q,p}}^{-1}), \quad (13)$$

where $\psi_{j,n}$ is the right eigenvector of the circuit Laplacian and E_j its corresponding eigenvalue. $\mathbf{J}_{\text{TE}}^{-1}$ is the (l, m) th element of the inverse of the admittance matrix [39,44]. To connect the impedance spectra to the evolution of the topological corner modes, we calculate the impedance $Z_{(x=1,y=1,A),(x',y',D)}$ between the A node of the unit cell at the lower left corner and the D node of the unit cell at the arbitrary coordinates (x, y) . We plot the impedance spectra of a system with 20 unit cells along the x and y directions under open boundary conditions. Interestingly, the impedance distribution in the untilted and untilted cases closely follows the spatial distributions of the eigenmodes with nearly zero admittance. As can be seen in Fig. 5(a), very large impedance values appear in the vicinity of one of the corners in the absence of long-range hopping ($C_N = 0$). The occurrence of these large impedance values can be explained by considering Eq. (12) and Fig. 3(a). Figure 3(a) shows that there exist nearly zero-admittance nontrivial modes. These modes dominate the impedance value in Eq. (12) because Z_{pq} is inversely proportional to the eigenenergies E_j . In contrast, a finite value of C_N with a magnitude smaller than C_N^{critical} induces a tilt in the admittance dispersion. As a result, most of the nontrivial modes shift to nonzero admittance [see Fig. 3(b)], and the bulk admittance band gap decreases. The impedance magnitude therefore falls sharply. Although the maximum impedance still occurs at the same corner, the two neighboring edges now also have significant magnitudes of impedance relative to that at the corner [see Fig. 5(b)].

Note that the impedance distributions follow that of the nearly zero-admittance modes (rather than just corner modes) in the type-I and type-II regimes of the system. This is because for the type-II regime [which is depicted in Fig. 3(b)], the nearly zero-admittance modes consist of both the corner mode as well as the edge mode. Both of these modes are in the vicinity of the zero-admittance line and lie approximately at the same distance from it [see Fig. 3(b)]. The corresponding impedance measurement shown in Fig. 5(b), which would

pick out the nearly zero eigenmodes, would thus have substantial contributions from both the corner and the edge modes. This is unlike the type-I regime, where the corner mode is the only eigenmode with close to zero admittance, while the edge modes lie significantly further away from the zero-admittance line [see Fig. 3(a)]. The corresponding impedance measurement [see Fig. 5(a)] shows localization only at one of the corners, indicating substantial contribution only from the corner mode. In summary, the type-I regime (contribution only from type-I corner mode) can be distinguished from that of the type-II regime (admixture of type-II corner mode and edge mode) by means of the impedance measurement.

Finally, when the magnitude of the NNN coupling is increased beyond that of the critical value (i.e., $|C_N| \geq |C_N^{\text{critical}}|$), the admittance band gap vanishes and the nontrivial corner modes mix with the bulk modes. As a result, the impedance spectra no longer exhibit corner localization but are instead randomly distributed along both spatial directions [see Figs. 5(c) and 5(d)].

E. Simulation with realistic components and experimental proposal

In this section, we examine the type-II corner modes by considering circuits with intrinsic resistances and realistic components via the LTspice electric circuit simulation software. Although the LC components are treated as ideal lossless circuits elements above, in realistic circuits, resistances due to the components themselves and the wiring are inevitable. To perform the circuit simulation, we used a 4-by-4 unit cell circuit with four nodes in each unit cell, as discussed above. We performed the simulation with 64 nodes, which is sufficient to evaluate the replicability of the type-II corner modes under realistic resistances. For the components connecting each pair of nodes link, we picked Würth Elektronik 885012208013 ($1 \mu\text{F} \pm 10\%$) for C_2 , Würth Elektronik 885012209002 ($0.22 \mu\text{F} \pm 10\%$) for C_N and Würth Elektronik 744025100 ($10 \mu\text{H} \pm 20\%$) for the common grounding

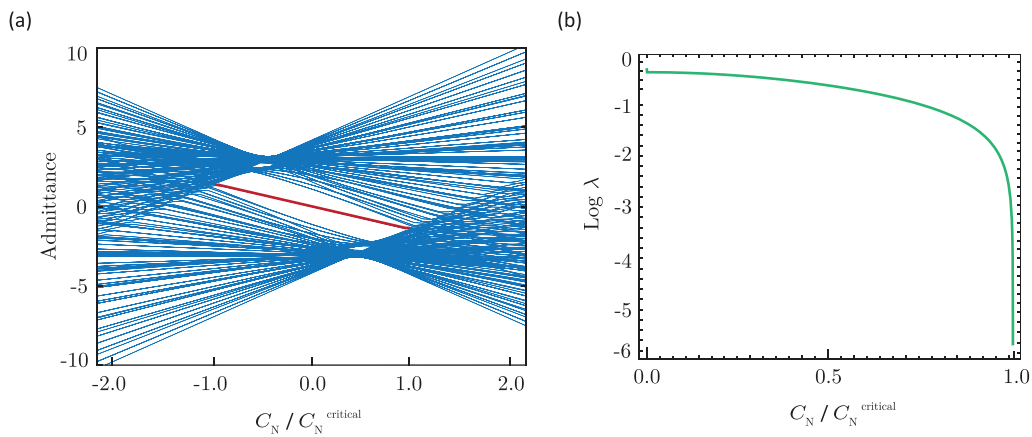


FIG. 4. Inverse localization characteristics of the type-II corner modes. (a) The admittance spectra of the TE circuit described in Eq. (1) under OBC with 10×10 unit cells in the x and y directions, which are plotted as functions of C_N with $C_1 = 1 \text{ mF}$, $C_2 = 2 \text{ mF}$. The thick magenta line denotes the corner modes. (b) Logarithmic inverse localization length of the corner modes, which is plotted as a function of the long-range hopping C_N at resonant frequency of $f = f_r = \frac{1}{2\pi} (\sqrt{2(C_1 + C_2 + 2C_N)}L)^{-1}$. Circuit parameters used: $C_1 = 1 \text{ mF}$, $C_2 = 2 \text{ mF}$. The corner modes exponentially fall near $C_N \approx C_N^{\text{critical}} = \frac{C_2}{2\sqrt{2}}$, where the vanishing of the admittance gap is accompanied by the mixing of the corner and bulk admittance modes.

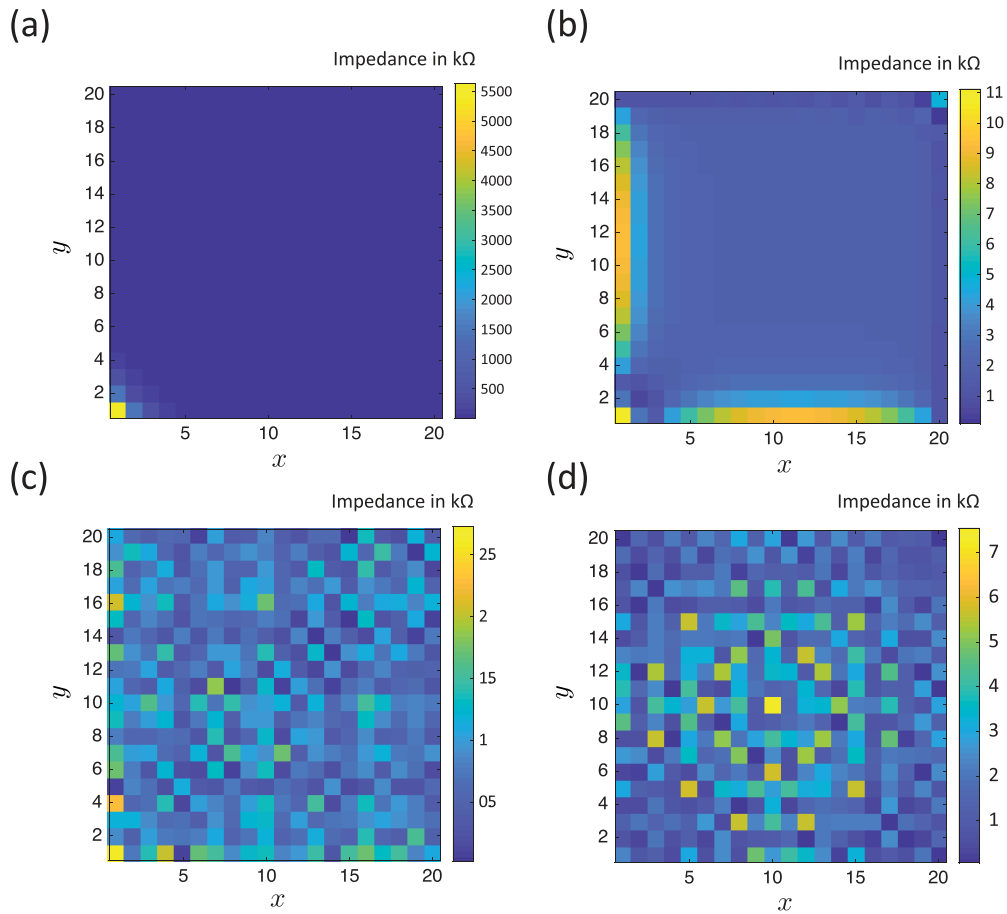


FIG. 5. Impedance spectra of the circuit described by Eq. (1) under OBC in x and y directions for different values of C_N . Note that each pixel in the plot corresponds to a unit cell containing four nodes, and not to each individual node. (a) Impedance $Z_{(x=1,y=1,A),(x',y',D)}$ for the higher-order TE lattice with NN interaction only (i.e. $C_N = 0$). The large impedance localization at the corner is due to the presence of the nearly zero-admittance corner modes. (b) $Z_{(x=1,y=1,A),(x',y',D)}$ for an undertilted higher-order TE system with $|C_N| < |C_N|^{\text{critical}}$ (i.e., $C_N = 0.15$ mF). The impedance is localized in the vicinity of one corner and neighboring edges. (c) and (d) $Z_{(x=1,y=1,A),(x',y',D)}$ for $C_N = C_N^{\text{critical}}$ (i.e., $C_N = 0.35355$ mF) in (c) and $C_N > C_N^{\text{critical}}$ (i.e., $C_N = 0.45$ mF) for (d). Note that the large impedance is no longer localized to a corner node because of the mixing between the bulk and corner modes. We consider a system size of 20×20 unit cells. The resonant frequency is set at $f = f_r = \frac{1}{2\pi}(\sqrt{2(C_1 + C_2 + 2C_N)L})^{-1}$. Common circuit parameters used: $C_1 = 0.5$ mF, $C_2 = 1$ mF, and $L = 100$ μ H.

inductors attached to every node to the ground from the LT-spice database. The tolerance values are sufficient to test the topological modes under notable variations. These specific components were chosen because of their low series resistances and their availability in the market. Theoretically, the effect of the series resistances can be modeled by replacing the couplings in the circuit Laplacian [Eq. (1)] with $(i\omega C)^{-1} \rightarrow (i\omega C + R_C)^{-1}$ for capacitors and $i\omega L \rightarrow i\omega L + R_L$ for inductors. According to the data sheet of the components chosen, the series resistances of the components are < 10 m Ω , which is much less than the theoretically calculated resistance values that may affect the topological modes. Because the admittance profile of the circuit under OBC along both directions is obtained by varying the intracell coupling capacitors C_1 in Fig. 3, we suggest the use of variable capacitors for the experimental realizations instead of using different circuits setups with different C_1 values. Using variable capacitors also reduces the risk of the variations that may possibly come with different components.

For the circuit simulation, we consider the C_1 couplings as variable capacitors and set their series resistance values as that of the C_2 capacitors (~ 6.5 m Ω Würth Elektronik 885012208013). The circuit admittance spectrum can be obtained through the circuit Laplacian, which relates the voltage response to the injected currents, i.e., $\mathbf{I} = J_{\text{TE}} \cdot \mathbf{V}$ where \mathbf{I} and \mathbf{V} are the matrices of the injected current and voltages at the nodes, respectively. Therefore, to obtain the circuit Laplacian through the simulation, we follow these steps: (i) We inject current with a constant magnitude at a circuit node and export the voltage responses of every node in the entire circuit, (ii) The exported voltage values are inserted to the corresponding matrix column of the voltage matrix. (iii) We then repeat this process by injecting current into a different node of the circuit in each iteration to build up the current and voltage matrices column by column until we obtain the full voltage matrix. (iv) The inverse of the voltage matrix gives us the circuit Laplacian (i.e., $J = \mathbf{V}^{-1} \cdot \mathbf{I}$). (v) The eigenvalue spectrum of the Laplacian obtained through the simulation yields the

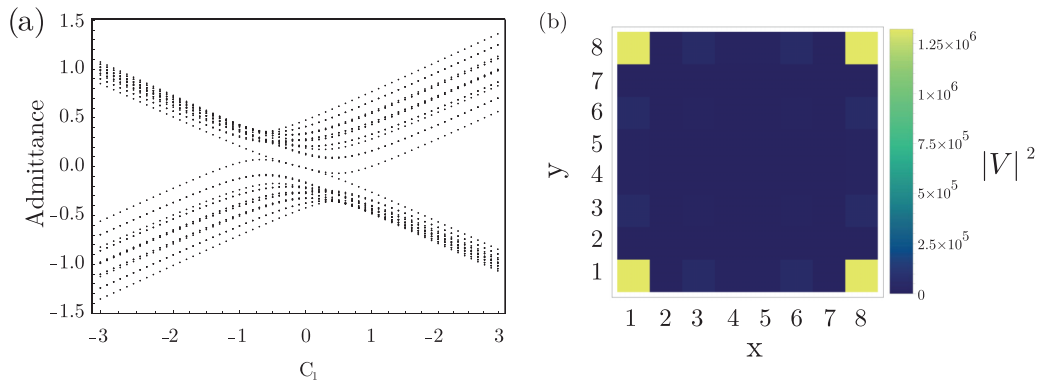


FIG. 6. Simulated admittance spectrum and the square of the voltage spatial distribution of type-II corner modes with 4×4 unit cells. (a) The admittance spectrum in the presence of the NNN couplings (C_N) was obtained using the LTspice electric circuit simulation software. For the simulation, the chosen component values and their documentation labels are $C_2 = 1 \mu\text{F}$ (Würth Elektronik 885012208013), $C_N = 0.22 \mu\text{F}$ (Würth Elektronik 885012209002), and $L = 10 \mu\text{H}$ (Würth Elektronik 744025100). The driving AC frequency is set at the resonant frequency of $f_r = 35.588 \text{ kHz}$. (b) The square magnitude of the voltage spatial distribution at $C_1 = 0.3 \mu\text{F}$. Even though the parasitic effects temper the magnitude of the voltage profile, the corner modes still efficaciously survive.

admittance spectrum. After all these steps, we observe that the simulated admittance spectrum [Fig. 6(a)] of our circuit depicted in Fig. 1(a) is in agreement with the theoretically calculated spectrum [Fig. 3(b)]. Our simulation therefore shows that the type-II corner modes still survive despite the presence of parasitic effects.

Beyond the simulations, experimental setups require more careful attention to realise such topological states. For example, parasitic effects arise not only because of the components themselves but can also be due to contact resistance and weldings. Besides the parasitic effects, the presence of active circuit elements such as operational amplifiers (OpAmps) may break the circuit because of energy pumping or sinking by the OpAmps. To protect the circuit from such effects, it is advisable to ground every node with a resistor that consumes sufficient energy but damps the energy pumping from the ground. The use of *high-speed, high-precision* OpAmps such as the LT1056 also ensures the circuit reaches stability quickly without allowing any voltage accumulation around defects. By considering such effects, the topological modes that our circuit hosts can be realizable in realistic circuits. Furthermore, the spatial distribution of the square of the magnitude of node voltage at $C_1 = 0.3 \mu\text{F}$ is plotted in Fig. 6(b), which shows the localization of corner modes at the corner nodes and the significant decrease in the voltage density at other nodes along the edges. Interestingly, even though the parasitic effects temper the magnitude of the voltage profile, the corner modes still dramatically survive [see Fig. 6(b)], indicating the robustness of the corner modes in our TE model against perturbations and system disorders.

III. CONCLUSION

In summary, we characterized higher-order topological phases (HOTPs) based on a topolectrical (TE) circuit model. In particular, we analyzed the emergence of a type-II corner mode in the presence of long-range interactions which are

realized in TE circuits by the introduction of next-nearest neighbor (NNN) coupling capacitances. Unlike the conventional type-I corner modes that are localized at the corner sublattice nodes with very large inverse decay lengths in the absence of long-range coupling, the type-II corner modes that emerge in the presence of long-range coupling, which breaks the chiral symmetry of the system, are localized on the corner nodes with a finite inverse decay length (e.g., much slower exponential decay). This results in a spread of the eigenstates density distribution towards the edges. The NNN coupling also induces a tilt in the admittance dispersion of the circuit, and beyond a critical value results in a transition to the over-tilted Dirac dispersion. This in turn leads to a hybridization of the bulk and corner modes, resulting in the disappearance of distinct corner modes. Furthermore, we numerically obtained the impedance between the lower-left corner of the system and arbitrary unit cells using the Green's function method. The impedance spectra of the different corner mode configurations exhibit different characteristics. More specifically, type-I and type-II corner modes can be distinguished by the corner and edgelike spatial distribution of their impedance, respectively. This impedance behavior reflects the zero-admittance non-trivial modes and tilted nonzero corner modes, respectively. We demonstrate the emergence of type-II topological corner modes based on the TE circuit framework, which unlike its condensed matter counterpart, allows ready implementation and fine tuning of the coupling strengths. Due to this flexibility, TE circuits provide an ideal platform to demonstrate unusual features of higher-order topological phases arising from long-range interactions, and to engineer and modulate their robust topological corner modes.

ACKNOWLEDGMENTS

This work is supported by the Ministry of Education (MOE) of Singapore Tier-II Grant MOE-T2EP50121-0014 (NUS Grant No. A-8000086-01-00), and MOE Tier-I FRC Grant (NUS Grant No. A-8000195-01-00).

- [1] R. Roy, *Phys. Rev. B* **79**, 195322 (2009).
- [2] T. Fujita, M. B. A. Jalil, S. G. Tan, and S. Murakami, *J. Appl. Phys.* **110**, 121301 (2011).
- [3] X. Zhang, B. Zhang, H. Sahin, Z. B. Siu, S. M. Rafi-UI-Islam, J. F. Kong, M. Jalil, R. Thomale, and C. H. Lee, [arXiv:2204.05329](https://arxiv.org/abs/2204.05329).
- [4] T. Senthil, *Annu. Rev. Condens. Matter Phys.* **6**, 299 (2015).
- [5] C. He, X. Ni, H. Ge, X.-C. Sun, Y.-B. Chen, M.-H. Lu, X.-P. Liu, and Y.-F. Chen, *Nat. Phys.* **12**, 1124 (2016).
- [6] C. Sun, S. M. Rafi-UI-Islam, H. Yang, and M. B. A. Jalil, *Phys. Rev. B* **102**, 214419 (2020).
- [7] B. Yang, Z.-X. Hu, C. H. Lee, and Z. Papić, *Phys. Rev. Lett.* **118**, 146403 (2017).
- [8] S. G. Tan, S.-H. Chen, C. S. Ho, C.-C. Huang, M. B. Jalil, C. R. Chang, and S. Murakami, *Phys. Rep.* **882**, 1 (2020).
- [9] B. Göbel, A. Mook, J. Henk, and I. Mertig, *Phys. Rev. B* **96**, 060406(R) (2017).
- [10] C. A. Akosa, O. A. Tretiakov, G. Tatara, and A. Manchon, *Phys. Rev. Lett.* **121**, 097204 (2018).
- [11] K. Terabe, T. Hasegawa, T. Nakayama, and M. Aono, *Nature (London)* **433**, 47 (2005).
- [12] M. B. A. Jalil and S. G. Tan, *Sci. Rep.* **4**, 5123 (2014).
- [13] S. Krinner, D. Stadler, D. Husmann, J.-P. Brantut, and T. Esslinger, *Nature (London)* **517**, 64 (2015).
- [14] R. Takahashi and S. Murakami, *Phys. Rev. Lett.* **107**, 166805 (2011).
- [15] B.-J. Yang and N. Nagaosa, *Nat. Commun.* **5**, 4898 (2014).
- [16] F. D. M. Haldane, *Rev. Mod. Phys.* **89**, 040502 (2017).
- [17] E. Witten, *Commun. Math. Phys.* **117**, 353 (1988).
- [18] F. D. M. Haldane and S. Raghu, *Phys. Rev. Lett.* **100**, 013904 (2008).
- [19] W. Gao, M. Lawrence, B. Yang, F. Liu, F. Fang, B. Béni, J. Li, and S. Zhang, *Phys. Rev. Lett.* **114**, 037402 (2015).
- [20] A. B. Khanikaev, S. H. Mousavi, W.-K. Tse, M. Kargarian, A. H. MacDonald, and G. Shvets, *Nat. Mater.* **12**, 233 (2013).
- [21] N. Goldman, J. C. Budich, and P. Zoller, *Nat. Phys.* **12**, 639 (2016).
- [22] G. Ma, M. Xiao, and C. T. Chan, *Nat. Rev. Phys.* **1**, 281 (2019).
- [23] Z. Yang, F. Gao, X. Shi, X. Lin, Z. Gao, Y. Chong, and B. Zhang, *Phys. Rev. Lett.* **114**, 114301 (2015).
- [24] Q. Cheng, Y. Pan, Q. Wang, T. Li, and S. Zhu, *Laser Photonics Rev.* **9**, 392 (2015).
- [25] M. Esmann and N. D. Lanzillotti-Kimura, *Appl. Sci.* **8**, 527 (2018).
- [26] V. Peano, C. Brendel, M. Schmidt, and F. Marquardt, *Phys. Rev. X* **5**, 031011 (2015).
- [27] M. Ezawa, *Phys. Rev. Lett.* **120**, 026801 (2018).
- [28] F. Schindler, A. M. Cook, M. G. Vergniory, Z. Wang, S. S. Parkin, B. A. Bernevig, and T. Neupert, *Sci. Adv.* **4**, eaat0346 (2018).
- [29] B.-Y. Xie, H.-F. Wang, H.-X. Wang, X.-Y. Zhu, J.-H. Jiang, M.-H. Lu, and Y.-F. Chen, *Phys. Rev. B* **98**, 205147 (2018).
- [30] S. Franca, J. van den Brink, and I. C. Fulga, *Phys. Rev. B* **98**, 201114(R) (2018).
- [31] H. Xue, Y. Yang, F. Gao, Y. Chong, and B. Zhang, *Nat. Mater.* **18**, 108 (2019).
- [32] C. W. Peterson, W. A. Benalcazar, T. L. Hughes, and G. Bahl, *Nature (London)* **555**, 346 (2018).
- [33] B.-Y. Xie, G.-X. Su, H.-F. Wang, H. Su, X.-P. Shen, P. Zhan, M.-H. Lu, Z.-L. Wang, and Y.-F. Chen, *Phys. Rev. Lett.* **122**, 233903 (2019).
- [34] X. Ni, M. Weiner, A. Alu, and A. B. Khanikaev, *Nat. Mater.* **18**, 113 (2019).
- [35] C. Poli, H. Schomerus, M. Bellec, U. Kuhl, and F. Mortessagne, *2D Mater.* **4**, 025008 (2017).
- [36] M. Li, D. Zhirihin, M. Gorkach, X. Ni, D. Filonov, A. Slobozhanyuk, A. Alù, and A. B. Khanikaev, *Nat. Photonics* **14**, 89 (2020).
- [37] X.-W. Xu, Y.-Z. Li, Z.-F. Liu, and A.-X. Chen, *Phys. Rev. A* **101**, 063839 (2020).
- [38] Y.-Z. Li, Z.-F. Liu, X.-W. Xu, Q.-P. Wu, X.-B. Xiao, M.-R. Liu, L.-L. Chang, and R.-L. Zhang, *Europhys. Lett.* **132**, 20005 (2020).
- [39] S. M. Rafi-UI-Islam, Z. B. Siu, C. Sun, and M. B. Jalil, *New J. Phys.* **22**, 023025 (2020).
- [40] S. Rafi-UI-Islam, Z. B. Siu, and M. B. Jalil, *Commun. Phys.* **3**, 72 (2020).
- [41] S. M. Rafi-UI-Islam, Z. B. Siu, H. Sahin, C. H. Lee, and M. B. Jalil, *Phys. Rev. Res.* **4**, 043108 (2022).
- [42] S. Imhof, C. Berger, F. Bayer, J. Brehm, L. W. Molenkamp, T. Kiessling, F. Schindler, C. H. Lee, M. Greiter, T. Neupert *et al.*, *Nat. Phys.* **14**, 925 (2018).
- [43] S. M. Rafi-UI-Islam, Z. B. Siu, and M. B. A. Jalil, *Phys. Rev. B* **103**, 035420 (2021).
- [44] C. H. Lee, S. Imhof, C. Berger, F. Bayer, J. Brehm, L. W. Molenkamp, T. Kiessling, and R. Thomale, *Commun. Phys.* **28**, 1 (2018).
- [45] H. Sahin, S. M. Rafi-UI-Islam, Z. B. Siu, C. H. Lee, and M. Jalil, *Bull. Am. Phys. Soc.* **4**, 043021 (2022).
- [46] S. Rafi-UI-Islam, Z. B. Siu, and M. B. Jalil, *Appl. Phys. Lett.* **116**, 111904 (2020).
- [47] N. A. Olekhno, E. I. Kretov, A. A. Stepanenko, P. A. Ivanova, V. V. Yaroshenko, E. M. Puhtina, D. S. Filonov, B. Cappello, L. Matekovits, and M. A. Gorkach, *Nat. Commun.* **11**, 1436 (2020).
- [48] S. M. Rafi-UI-Islam, Z. B. Siu, and M. B. Jalil, *New J. Phys.* **23**, 033014 (2021).
- [49] T. Hofmann, T. Helbig, C. H. Lee, M. Greiter, and R. Thomale, *Phys. Rev. Lett.* **122**, 247702 (2019).
- [50] S. M. Rafi-UI-Islam, Z. B. Siu, H. Sahin, C. H. Lee, and M. B. A. Jalil, *Phys. Rev. Res.* **4**, 013243 (2022).
- [51] T. Ozawa, H. M. Price, A. Amo, N. Goldman, M. Hafezi, L. Lu, M. C. Rechtsman, D. Schuster, J. Simon, O. Zilberberg *et al.*, *Rev. Mod. Phys.* **91**, 015006 (2019).
- [52] S. D. Huber, *Nat. Phys.* **12**, 621 (2016).
- [53] C.-A. Li and S.-S. Wu, *Phys. Rev. B* **101**, 195309 (2020).
- [54] B. Pérez-González, M. Bello, Á. Gómez-León, and G. Platero, *Phys. Rev. B* **99**, 035146 (2019).
- [55] L.-Y. Zheng, V. Achilleos, O. Richoux, G. Theocharis, and V. Pagneux, *Phys. Rev. Appl.* **12**, 034014 (2019).
- [56] W. A. Benalcazar, B. A. Bernevig, and T. L. Hughes, *Science* **357**, 61 (2017).
- [57] W. A. Benalcazar, B. A. Bernevig, and T. L. Hughes, *Phys. Rev. B* **96**, 245115 (2017).

- [58] D. Obana, F. Liu, and K. Wakabayashi, *Phys. Rev. B* **100**, 075437 (2019).
- [59] C. Yesilyurt, Z. B. Siu, S. G. Tan, G. Liang, S. A. Yang, and M. B. Jalil, *Sci. Rep.* **9**, 4480 (2019).
- [60] C. Yesilyurt, Z. B. Siu, S. G. Tan, G. Liang, S. A. Yang, and M. B. Jalil, *Appl. Phys. Lett.* **111**, 063101 (2017).
- [61] A. Kundu, Z. B. Siu, H. Yang, and M. B. Jalil, *New J. Phys.* **22**, 083081 (2020).
- [62] S. M. Rafi-Ul-Islam, Z. B. Siu, C. Sun, and M. B. A. Jalil, *Phys. Rev. Appl.* **14**, 034007 (2020).
- [63] O. Viyuela, D. Vodola, G. Pupillo, and M. A. Martin-Delgado, *Phys. Rev. B* **94**, 125121 (2016).
- [64] R. Ball, *Phys. Rev. Lett.* **95**, 176407 (2005).
- [65] R. G. Dias and A. M. Marques, *Phys. Rev. B* **105**, 035102 (2022).
- [66] X.-F. Zhang, S.-F. Tian, and J.-J. Yang, *arXiv:2109.02901*.